LETTER

Origin and implications of non–radial Imbrium Sculpture on the Moon

Peter H. Schultz[1] & David A. Crawford[2]

Rimmed grooves, lineations and elongate craters around Mare Imbrium shape much of the nearside Moon. This pattern was coined the Imbrium Sculpture[1], and it was originally argued that it must have been formed by a giant oblique (∼30°) impact, a conclusion echoed by later studies[2]. Some investigators, however, noticed that many elements of the Imbrium Sculpture are not radial to Imbrium, thereby implicating an endogenic or structural origin[3,4]. Here we use these non-radial trends to conclude that the Imbrium impactor was a proto-planet (half the diameter of Vesta), once part of a population of large proto-planets in the asteroid belt. Such independent constraints on the sizes of the Imbrium and other basin-forming impactors markedly increase estimates for the mass in the asteroid belt before depletion caused by the orbital migration of Jupiter and Saturn[5]. Moreover, laboratory impact experiments, shock physics codes and the groove widths indicate that multiple fragments (up to 2% of the initial diameter) from each oblique basin-forming impactor, such as the one that formed Imbrium, should have survived planetary collisions and contributed to the heavy impact bombardment between 4.3 and 3.8 billion years ago.

Previous interpretations for the Imbrium Sculpture included expressions of both structural features and secondary ejecta[6,7]. Horsts and graben crossing the Imbrium basin rim (the Apennine Mountains)[6] and subsurface radial dikes detected from Gravity Recovery and Interior Laboratory (GRAIL) data[8] support this interpretation in certain locations. Most of the features comprising the facies surrounding Imbrium, however, relate to ballistic emplacement[9,10]. Grooves and secondary craters with breached down-range rims record the momentum of ballistic debris but many do not radiate from the centre of the basin. Moreover, grooves that radiate from near the basin centre superpose those non-radial grooves and lineations originating well up range (Fig. 1a), in contrast to the traditional single-stage sequence of ejecta emplacement where the ejecta curtain advances outward systematically[10]. Rimmed grooves (sculptured terrains) characterize first-arriving debris, whereas lower-relief radial lineations (mobilized ejecta deposits) and elongated secondaries generally characterize late-arriving ejecta. Previous studies combined both facies into the single term Imbrium Sculpture, but differences in expression, direction and scale suggest that part of the sculpturing component (as originally described in Earth-based telescopic observations) may have a different cause.

The distribution of basin and ejecta asymmetries (see Extended Data Figs 1–4) indicates a northwest–southeast Imbrium-impactor trajectory[1,2]. Mapped endpoints of each groove/secondary (lineation) defined great circles that were traced back until they intersected the great circle delineating the impactor trajectory. The selected northwest–southeast trajectory was then readjusted until all great circles from Imbrium-related ejecta converged within the basin. Sets of these great circles were then subdivided according to where they crossed the readjusted trajectory line: up range from the basin centre, down range from the centre, and within a radius of 300 km around the centre. Laboratory and hydrocode impact experiments previously documented evolving

source regions where the ejecta launch positions migrated within the growing excavation crater (see Extended Data Fig. 5)[11–13]. The pattern becomes most evident when the impactor-diameter to crater-diameter ratio becomes large, for example, very large scales, oblique trajectories, strength-controlled targets or low-speed impacts. The pattern far to the east resembles one side of a butterfly pattern (the western counterpart masked by Oceanus Procellarum and Orientale ejecta) that reaches the lunar far side, about 2,700 km (90°) east of Mare Marginis. One set of lineations, however, never converges within the basin rim and parallels the optimized trajectory (Fig. 1b). We propose that this set is an expression of the failed impactor. Maps of the different sets of groove and lineation trends are included in Extended Data Figs 2–4.

Hypervelocity impact experiments[11,12] and numerical models[13] reveal sets of ejecta trajectories converging well up range of the final crater centre, just as is observed for Imbrium. In impact experiments (∼5 km s^{-1} at 15°) with solid targets, rays and surface scouring down range subtend an angle to either side of the trajectory comparable to the impact angle (Fig. 2b). The outermost set converges up range of the final crater rim and relates to the sheared-off portions of the impactor[13,14]. Nearly parallel scours, however, originate from either side of the projectile (Extended Data Fig. 6). For large-body impacts, surface curvature becomes important, and portions of the projectile escape re-impacting the surface entirely (Fig. 2b). Captured fragments, crater sizes in down-range witness plates, and in-flight imaging in laboratory experiments (see also Extended Data Fig. 7) reveal that 5–8 large, intact and unmelted fragments survive, which is indicative of a non-catastrophic failure process[15]. Collectively, the larger fragments comprise about half the initial mass, each of which represents 40–46% of the original impactor diameter.

This observed physical process in the laboratory should apply at much larger scales. A numerical simulation used the CTH shock-physics analysis package for a 100 km monolithic dunite asteroid hitting the Moon at an impact velocity of 10 km s^{-1} at 30° from horizontal and incorporating a localized shear-failure material model (see Methods). Just as in experiments, projectile components scour the surface down range well before crater excavation and ejecta emplacement; moreover, their trajectories can be traced back to the projectile at the region of first contact, with some sets that extend back to the sides of the original impactor (Fig. 3a). This simulation closely matches the orientation of mapped grooves around the Moscoviense basin on the Moon (Fig. 3b and Extended Data Fig. 8b).

Consequently, grooves and lineations comprising the Imbrium Sculpture reveal several important clues about the excavation process. First, the initial stage of excavation originated well up range of the basin centre, consistent with experiments and numerical models. Debris ejected at this stage has very high speeds and low angles directed generally down range[11,12]. Second, sheared-off (decapitated) portions of the original asteroid retain speeds close to its original impact speed and extend far down range due to surface curvature[15–18]. Proposed remnants include heavily degraded elongate craters and grooves

[1]Brown University, Department of Earth, Environmental, and Planetary Sciences, 324 Brook Street, Providence, Rhode Island 02912, USA. [2]Sandia National Laboratories, P. O. Box 5800, MS 0840, Sandia National Laboratories, Albuquerque, New Mexico 87185, USA.
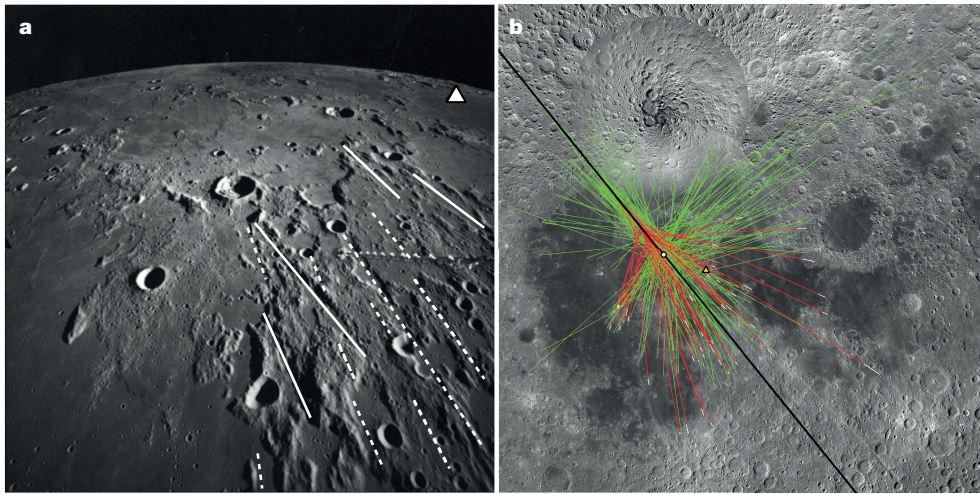
Figure 1 | Views and trends of Imbrium Sculpture. a, Imbrium Sculpture from south of the 24-km-diameter crater Lalande in the centre of view (looking to the northwest) with the crater Mösting at the top right. Dashed white lines trace secondaries originating from near the basin centre cross or truncate grooves originating well up range from the centre of Imbrium (solid lines). Triangle identifies the Surveyor 6 landing site in Sinus Medii (top right). Apollo 16 metric frame (A16-M-1413). **b**, Convergence of all grooves and highly elongated secondary craters on an Imbrium-centred map in a Lambert-stereographic conformal projection centred on Imbrium (offset from centre here). Yellow triangle locates the Apollo 15 landing site just inside the southeast Imbrium rim (white dot). Green lines correspond to subsets that converge along a great circle northwest of the basin centre. Red lines correspond to elongate secondaries converging up range of the basin centre, but a notable set of near-parallel trends up range (green) never converges within the basin. Black line indicates the proposed trajectory of the Imbrium impact (from the northwest); white dot indicates the basin centre. Image is a re-projected composite from the wide-angle Lunar Reconnaissance Orbiter Camera (LROC; circular region at top is an artefact around the North Pole). Sample size was determined by the ability to discern a clear orientation (based on length and expression) of each groove or elongated secondary crater, yielding over 230 mapped orientations (total set shown in Extended Fig. 3a).

beyond the southern rim of Imbrium (for example, Boscovich). Last, ejecta during later crater excavation stage (created by shock rarefactions off the free surface) become more radial to the centre of the final basin and superpose scouring from the earliest stages. Whether caused by ballistic ejecta from low-speed impacts or grazing impactor fragments, the width of each groove or crater should be
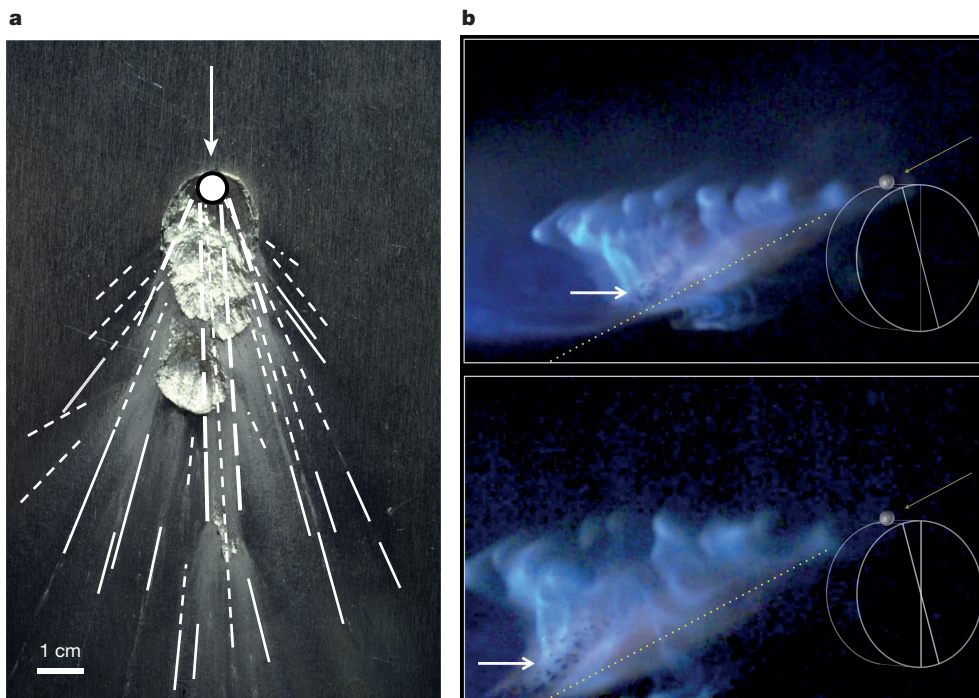
Figure 2 | An oblique impact experiment into a planar aluminium and cylindrical target by aluminium projectile impacting at $5.2\,km\,s^{-1}$. a, Scours originating from the point of first contact converge up range and result from projectile fragments re-impacting the surface downrange (impact angle was at 15° from the horizontal). **b**, An oblique impact into a curved surface prevents fragments from re-impacting the surface, as in planar targets. Fragments (arrows) surviving a $5\,km\,s^{-1}$ impact into a 6.7-cm aluminium disk (faintly outlined) by a 0.635-cm aluminium sphere (represented graphically). About $40\,\mu s$ after impact (top), down-range fragmental debris (just above the yellow dotted line) separates from the vapour plume (blue) along the initial trajectory. The bottom image shows the evolution $15\,\mu s$ later with 8–10 large fragments (1–3 mm across) travelling close to the same speed as the initial impactor. Additional images can be found in Extended Data Fig. 7. The experiments shown here have been replicated numerous (more than 30) times for both similar and different conditions of impactor speed and angle.
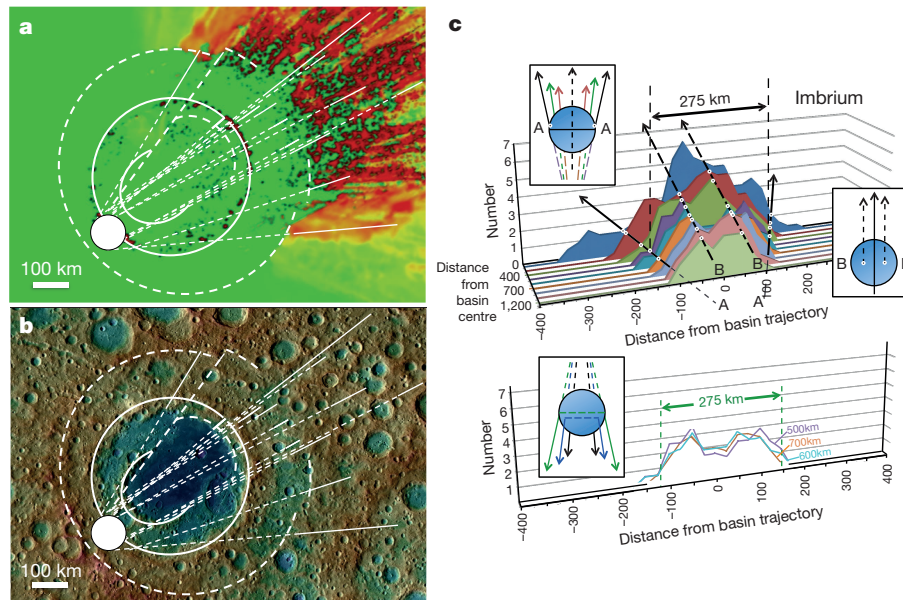
Figure 3 | Hydrocode simulation tracing impactor fragments from a basin-forming impact compared with scours from the Moscoviense basin. a, Hydrocode simulation of a 100 km asteroid impacting the Moon at 30° (dunite at 10 km s^{-1}) resulting in the same non-radial pattern observed in hypervelocity impact experiments. Red coloration is the pattern of asteroid relics interacting with the target surface. **b**, Mapped scours (degraded) on the Moscoviense basin for comparison with the hydrocode model. Images without overlays are included in the Extended Data Fig. 8. **c**, Histograms generated from intersections between great circles extending a subset of grooves (not converging within Imbrium) and great circles orthogonal to the Imbrium trajectory at different distances

from the basin centre (out to 1,200 km). Top view shows all sets between 400 km and 1,200 km from the basin centre, with down range to the top. The limits of intersections correspond to the sides of the projectile (A–A and B–B in the insets). Bottom view selects just those intersections between 500 km and 700 km from the basin centre where the impact point occurred. The diameter of the Imbrium impactor is estimated to have been between 220 km and 275 km in diameter. See also Extended Data Fig. 2d. Intersection points composing the histograms have observational errors that depend on the length and distance of the measured grooves and scours. Repeat measurements indicate errors no more than 30 km.

controlled by the target strength and only a few times the size of the impacting debris (see Methods).

Such observations indicate that debris scoured the surface down range before reaching the final transient cavity dimension, well before the arrival of ejecta from the excavation stage. Expressions of pre-ejecta scouring include breaches in the southeast Imbrium rim within the Apennines and the arcuate region southeast of Imbrium (extending from craters Julius Caesar to near Flamarian). Similarly, the extension of the inner ring and degraded scour zones crossing the outer ring in Moscoviense illustrate this process (Fig. 3b), in contrast with the up-range rim[17].

The evolving flow field from an oblique impact accounts for the different groove orientations and enigmatic sequence of the Imbrium Sculpture. On the basis of experiments and models, certain sets of Sculpture probably originated from surviving impactor fragments and can be used to constrain the size of the Imbrium projectile, provided the Imbrium impact point can be determined. The farthest up-range location of the impact point must be well within the outermost Imbrium ring to the north (outer edge of Mare Frigoris). Groove trends up range intersecting the Imbrium trajectory line, however, constrain the farthest down-range location for the impact point, close to Montes Jura (Fig. 1b).

To provide a quantitative estimate for the Imbrium impactor size, great circle segments were placed orthogonal to the trajectory at incremental distances up range from the basin centre, as illustrated in laboratory experiments (Extended Data Figs 2–4). Intercepts between the extended great circles and this series of orthogonal lines generate a histogram as a function of distance from the basin centre (Fig. 3c). Those trends never crossing the original Imbrium trajectory originated from the sides of the impactor that detached soon after the moment of impact. On the basis of this strategy, the diameter of the Imbrium asteroid is estimated to have been 275 km, with statistical (and measurement) uncertainty constraining the outermost limit. If the

shoulder of the distribution is used, then the derived diameter reduces to 220 km. The best determination between these two values becomes $\sim$250 km $\pm$ 25 km. With the same approach, preliminary data indicate that the impactor diameters for the Schrödinger, Moscoviense and Orientale basins were $\sim$45 km, $\sim$100 km and $\sim$110 km, respectively[17].

The derived impactor diameters can be used to calculate the diameter of the apparent transient crater (see Methods). The apparent transient diameter here refers to the diameter measured at the pre-impact surface before collapse. For a non-porous, gravity-controlled scaling[19], the Imbrium body (250 km in diameter) impacting at 30° (25 km s^{-1}) would result in a pre-collapse apparent transient diameter of $\sim$850 km (compared to the observed diameter of $\sim$1,250 km) and closely corresponds to the next most inner ring, from Montes Alpes to inside the Archimedes plateau. Decreasing the impact speed to 15 km s^{-1} decreases the transient crater sizes to $\sim$700 km.

This reinterpretation of some components of the Imbrium Sculpture leads to other insights including impact speed, impactor signatures and sizes of proto-planets in the early Solar System. First, the derived sizes for the Orientale and Moscoviense impactors are nearly the same size, yet their basin diameters are very different (930 km and 445 km). Since both were formed by oblique impacts, this difference in crater size now requires a low impact speed for Moscoviense, consistent with the hydrocode model (Fig. 3b).

Second, impactor components surviving impact provide an explanation for meteoritic signatures within certain basins and highland lunar samples (see Methods). A previous study suggested that portions of the impactor could survive low-speed vertical impacts (based on a two-dimensional model)[20]. Here we find that the three-dimensional hydrocode model indicates that impactor components should line the basin interior but were buried by late-arriving ejecta beyond the rim. Down-range dispersal of the Imbrium impactor also could account for similar meteoritic compositions in Apollo 16 regolith breccias[21].

Last, Imbrium is among the largest among all lunar basins created during the Late Heavy Bombardment (LHB) between 4.1 and 3.7 billion years ago. On the basis of our independent estimate for its diameter, the Imbrium impactor would have been $\sim 2.5 \times 10^{22}$ g (for an asteroid with a bulk density of $2.5\,g\,cc^{-1}$). Consequently, the total mass intersecting just the Moon during the LHB significantly exceeded the 10^{21} g previously proposed[5]. But the Imbrium impactor was only one of many proto-planets in the proposed E-belt, which was destabilized by late giant planet migration[22]. Large-body oblique impacts on both the terrestrial planets and asteroids should have generated large debris injected into planet-crossing orbits due to surface curvature, for example, Rheasilvia on Vesta, Hellas on Mars, Crisium, and even the earlier South Pole–Aitken basin[18] on the Moon. Fragments as large as 2% of the original diameter survived these collisions (see Methods) and generated numerous multi-kilometre-size objects in planet-crossing orbits that would have led to numerous craters 20–50 km in diameter.

Online Content Methods, along with any additional Extended Data display items and Source Data, are available in the online version of the paper; references unique to these sections appear only in the online paper.

1. Gilbert, G. K. The Moon's face: a study of the origin of its features. *Science* **21,** 305–307 (1893).
2. Baldwin, R. B. *The Measure of the Moon* (Univ. of Chicago Press, 1963).
3. Hartmann, W. K. Radial structures surrounding lunar basins, I: the Imbrium System. *Commun. Lunar Planet. Lab.* **2,** 1–16 (1964).
4. Strom, R. G. Analysis of lunar lineaments, I: tectonic maps of the Moon. *Commun. Lunar Planet. Lab.* **2,** 205–216 (1964).
5. Gomes, R., Levison, H. F., Tsiganis, K. & Morbidelli, A. Origin of the cataclysmic Late Heavy Bombardment period of the terrestrial planets. *Nature* **435,** 466–469 (2005).
6. Spudis, P. D. *The Geology of Multi-Ring Impact Basins* (Cambridge Univ. Press, 1993).
7. Wilhelms, D. E. Secondary impact craters of lunar basins. *Proc. Lunar Planet. Sci. Conf.* **7,** 2883–2901 (1976).
8. Andrews-Hannah, J. C. *et al.* The structure and evolution of the lunar Procellarum region as revealed by GRAIL. *Nature* **514,** 68–71 (2014).
9. Wilhelms, D. E. *The Geologic History of the Moon* Professional Paper 1348 (US Geological Survey, 1987).
10. Oberbeck, V. R. The role of ballistic erosion and sedimentation. *Rev. Geophys. Space Phys.* **13,** 337–362 (1975).
11. Anderson, J. L. B., Schultz, P. H. & Heineck, J. T. Asymmetry of ejecta flow during oblique impacts using three-dimensional particle image velocimetry. *J. Geophys. Res.* **108,** 5094 (2003).
12. Hermalyn, B., Schultz, P. H. & Heineck, J. T., Early-stage coupling for oblique impacts into granular material. *41st Lunar Planet. Science Conf.* Abstract no. 2565 (2010).
13. Schultz, P. H. & Wrobel, K. Downrange impact melt and related effects from Hale Crater on Mars. *J. Geophys. Res.* **117,** E04001 (2012).
14. Schultz, P. H. & Gault, D. E. Prolonged global catastrophes from oblique impacts. *Spec. Pap. Geol. Soc. Am.* **247,** 239–261 (1992).
15. Crawford, D. A. & Schultz, P. H. A model of localized shear heating with implications for the morphology and paleomagnetism of complex craters. *Large Meteorite Impacts Planet. Evol. V* 047 (2013).
16. Schultz, P. H., Stickle, A. M. & Crawford, D. A. Effect of asteroid decapitation on craters and basins. *43rd Lunar Planet. Science Conf.* Abstract no. 2428 (2012).
17. Schultz, P. H. & Crawford, D. A. Lunar basin-forming projectiles. *45th Lunar Planet. Science Conf.* Abstract no. 1961 (2014).
18. Schultz, P. H. & Crawford, D. A. Origin of the nearside structural and geochemical anomalies on the Moon. *Spec. Pap. Geol. Soc. Am.* **477,** 141–159 (2011).
19. Schmidt, R. M. & Housen, K. R. Some recent advances in scaling of impact and explosion cratering. *Int. J. Impact Eng.* **5,** 543–560 (1987).
20. Yue, Z. *et al.* Projectile remnants in central peaks of lunar impact craters. *Nature Geosci.* **6,** 435–437 (2013).
21. Joy, K. H. *et al.* Direct detection of projectile relics from the end of the lunar basin-forming epoch. *Science* **336,** 1426–1429 (2012).
22. Bottke, W. F. *et al.* An Archeaean heavy bombardment from a destabilized extension of the asteroid belt. *Nature* **485,** 78–81 (2012).

Author Contributions P.H.S. conceived the idea and collected data for the Moon as well as the experiments; D.A.C. performed the shock physics model; P.H.S. and D.A.C. co-wrote the paper.

Author Information Reprints and permissions information is available at www.nature.com/reprints. The authors declare no competing financial interests. Readers are welcome to comment on the online version of the paper. Correspondence and requests for materials should be addressed to P.H.S. (peter_schultz@brown.edu).

METHODS

Imbrium grooves and elongated secondary craters. The Imbrium Sculpture reflects a sequence of arrival and source regions from Imbrium, even in the same region of the Moon, as illustrated by several examples. For reference, Extended Data Fig. 1 identifies the concentric rings of Imbrium defined by relic mountains and wrinkle ridges. The northern part of the outer ring (corresponding to Mare Frigoris) is poorly expressed due to collapse of the up-range rim. Extended Data Figure 2a includes a region southeast of Imbrium, close to the proposed trajectory. Farther west in this region, trends of some grooves diverge, trending more to the northwest. Extensions of these trends converge (and indicate a source) up range of the basin centre, characteristic of oblique impacts. This contrast in source regions becomes more apparent farther southwest (Extended Data Fig. 2b) and southeast of Imbrium (Extended Data Fig. 2c). Flow lines directed more radial to the basin centre overlap those secondaries and grooves originating up range. Up range from Imbrium (Extended Data Fig. 2d), grooves are narrower and closer to the basin than in other directions and also exhibit different source regions within the basin.

Expression of the initial trajectory for each set varies with impact angle. At higher impact angles (>45°), returning ejecta create slightly elongate craters. At lower angles (<30°), they produce elongate secondary craters with breached down-range rims, as down-range-directed debris interferes with excavation. At very low impact angles (10°), however, speeds need to increase in order to achieve a given ballistic range, thereby scouring the surface and producing rimmed grooves and scours that retain signatures of their initial momentum. The long grooves and elongated secondaries comprising the Imbrium Sculpture indicate that the impact angles must have been at very low angles (<10°).

Complete distribution of grooves and elongated secondary craters. The entire set of mapped grooves and elongated secondary craters with extensions along great circles towards Imbrium (Extended Data Fig. 3a). Some secondaries northeast of Mare Marginis (lateral) originate from a region up range of the basin centre. No statistical methods were used to predetermine the sample size. Many trends that converge up range from the basin centre are shown in Extended Data Fig. 3b. Source regions for a subset of grooves and elongate secondaries found up range of Imbrium cross the trajectory line well up range of the basin centre (illustrated in Fig. 1b and Extended Data Fig. 3c) and constrain the region of first contact by the Imbrium impactor to a region northwest of Sinus Iridum in what is now Mare Frigoris. Most trends, however, converge within 300 km of the centre of Imbrium (Extended Data Fig. 3d). The extended ballistic ranges to the east–northeast give the impression of a butterfly pattern, characteristic of an oblique impact, whereas the paucity of examples west and southwest reflect burial by later volcanic units of Oceanus Procellarum.

Some mapped sets indicate a source region down range of the basin centre as the result of a migrating ejecta flow centre. Such flow migration characterizes the early stages of oblique impacts and becomes more evident at very large scales as cratering efficiency reduces due to the role of gravity limiting crater growth. A subset of trends, however, never crosses the trajectory line or converges beyond the up-range rim of Imbrium (Extended Data Fig. 4). These sets are interpreted as grooves and secondary craters created by decapitated fragments from the Imbrium impactor and are used to constrain estimates for its size. Those great circles delineating the lateral limit represent fragments from the sides of the impactor, whereas those close to the trajectory are from the top. We suggest that a portion of Rheita Vallis is actually associated with Imbrium, rather than Nectaris. A fraction of the initial kinetic energy is lost during large-body oblique impacts. In laboratory experiments[14] (at 5 km s^{-1} to 6 km s^{-1}), as much as 22% at 15° and 10% at 30° of the initial kinetic energy decouples from crater formation in planar impacts. Curved surfaces allow impactor debris to extend farther beyond the rim (or lost to space, if not re-accreted) before impacting the surface (shown in Fig. 2b). Such decoupling results in dramatic reductions in crater depth, in evidence from both laboratory experiments and numerical codes[18].

Late-stage ejecta typically bury or mask earlier stages originating up range. Ejecta from Imbrium, however, are not simply deposited but are mobilized after striking the surface due to their initial momentum, thereby resulting in extensive mixing[10]. Hence, deposit thicknesses are difficult to measure, if not predict. Mapping of the different sets directly down range (near Julius Caesar; Extended Data Fig. 2c) illustrates such burial or extensive modification. In other directions (Extended Data Fig. 2a), ejecta deposits may stagnate in lows, which exposes crossing patterns at higher elevations (for example, Sinus Aestuum, near the horizon in Fig. 1a). At greater distances from Imbrium, thinning of the ejecta deposits allows recognition of the different orientations more clearly (Extended Data Fig. 2b).

Strategy for determining impact first contact and impactor size. Laboratory impact experiments capture ejecta in ballistic flight through a pulsed laser sheet[11]. Extended Data Figure 5 illustrates the evolution of ejecta trajectories as they evolve during crater growth and clearly reveals that the source region for ejecta evolves from a position near the impact point (Extended Data Fig. 5a, red dot) to a position

close to the centre of the final crater (Extended Data Fig. 5b). In laboratory-scale experiments using loose particulates, the size of the region of coupling between the projectile and target is small relative to the final crater, best expressed at early stages of formation[11,12]. Specifically, the ratio between crater diameter and projectile diameter ranges from 20:1 to 50:1, depending on impact angle and impact speed. For strength-controlled targets (Fig. 2a), however, this ratio ranges from 4 to 8, also depending on angle and speed. This ratio reduces as a function of increasing size for gravity-controlled growth[19] and approaches that for a strength-controlled crater at basin scales. Hence, the evolving source region establishes a strategy not only for determining the point of impact but also constrains the size of the projectile, provided that the crater-to-projectile diameter ratio is small as illustrated in Fig. 2.

The point of first contact is constrained by the convergence of up-range ejecta, whereas the size of the projectile can be determined from the convergence of the down-range ejecta (Extended Data Fig. 6a). Such pronounced asymmetries disappear through time in laboratory experiments using gravity-controlled particulate targets (Extended Data Fig. 5b). Trends established by scouring extend up range, where they cross two orthogonal lines placed at different distances from the up-range rim for both a 15° and 30° impact (Extended Data Fig. 6b). Crossing the orthogonal line at the up-range crater rim provides a reasonable prediction for the projectile diameter. In these images, the slight offset from the trajectory line is the result of the spin of the projectile due to rifling in the launch tube. This spin imparts a centrifugal force to sheared and spalled fragments as demonstrated by reversed offsets between left- and right-hand twist tubes.

A subset of trends of impacting ejecta (grooves and elongate craters) northwest of Imbrium (up range) converges within the Atlas Mountains, but none originates northward of Mare Frigoris (Extended Data Fig. 3c). Consequently, the region of first contact must be confined to this region (Extended Data Fig. 3a). Those great-circle trends determined from inferred down-range ejecta trajectories, extending back to the region of first contact, then can be used to constrain an estimate for the lateral dimension of the object that formed this basin, independent of any a priori information about the impact angle or speed (only the trajectory needs to be assumed or determined). Results of the CTH moel of the Moscoviense impact further justify this strategy (Fig. 2b).

CTH model. The average impact speed by asteroids at the Moon is ~23 km s^{-1}, but for this numerical simulation (Fig. 3a) we assumed a relatively low-speed impact to demonstrate that the process does occur at much larger scales (and at only slightly higher speeds than in the experiments). The CTH model[23] will be described more fully in a separate contribution but is summarized elsewhere[15]. This new modification includes a damage model[24] incorporating the pressure-dependent melt curve[25]. Specifically, the yield strength of fully damaged material follows a Coulomb friction law. As conditions approach the melting point, thermal softening of the bulk material occurs. The model also included a method to estimate strain-dependent statistical crack spacing, shear heating within cracks, and heat loss via conduction away from cracks. As the temperature within a crack approaches the melting temperature, these additions now incorporate thermal softening. The combination of these modifications to the code results in a Brittle Damage with Localized Thermal Softening (BDL) model. This model depends on crack spacing (L), which is assumed to follow a power law in strain rate ($\dot{\varepsilon}$), that is, $L = L_0 \dot{\varepsilon}^{-n}$.

Here we chose L_0 and n to produce crack spacing of 2–7 m for strain rates encountered during formation of terrestrial craters with diameters of 1–280 km. The BDL model predicts thermal crack widths of 0.3–3 cm and characteristic cooling times of 10–1,000 s for the equation of state (EOS), strength and conductivity properties appropriate for silicates. Frictional heating within each crack is proportional to $\mu L \dot{\varepsilon} P$, where μ is the friction coefficient (which decreases with temperature) and P is pressure. With the crack spacing and widths used here, 0.1–1% of rock volume is affected by this process. Surface curvature is an important factor for tracking the fate of decapitated projectile fragments from the formation of a basin the size of Imbrium, but such a model would be computationally expensive. Instead, we modelled the Moscoviense impact to demonstrate the basic processes, sequence of arrival, and migrating source regions for impactor debris.

Basin scaling. With the determined impactor size and reasonably constrained impact angle (20° to 30°), well-established crater scaling relations[19] can be used to estimate the size of the transient (pre-collapse) cavity for Imbrium, both for consistency and comparison with observable surface features.

$$D_{\mathrm{g}}/2r = (\rho/\delta)^{1/3} k [(v\sin\theta)^2/gr]^{\alpha/3} \qquad (1)$$

Variables are defined as the following: D_{g}, transient crater diameter limited by gravity; r, impactor radius; ρ, projectile density; δ, lunar density; v, impact speed; θ, impact angle from the horizontal; k, an empirically derived material-dependent constant; α, an exponent dependent on the relative role of momentum and gravity controlling excavation; and g, gravitational acceleration of the Moon. The chosen

exponents and constants are based on experimental values for near-gravity scaling for loose particulates[26] with the following: $\alpha = 0.51$; and $k = 1.07$, a constant (including a shape factor for the diameter). The basis for this approach is that the initial collision generates a strong shock that converts the target into loose material under extension during the excavation stage. Wet sand scaling also has been used to represent gravity-controlled growth of non-porous materials[19] with the same dimensionless scaling equation but different values for the exponent ($\alpha = 0.65$) and constant ($k = 0.8$). These two approaches bracket the extrapolations. The average speed impact speed for the Moon today is around $23\,\mathrm{km\,s}^{-1}$ but uncertainties require consideration of a range of possibilities. Comparison between these two scaling relations and the range of impact speeds is summarized in Extended Data Table 1.

The two scaling approaches yield similar values of $\sim$830–860 km ($25\,\mathrm{km\,s}^{-1}$) and $\sim$700 km ($15\,\mathrm{km\,s}^{-1}$) for the Imbrium transient apparent diameter (different from the final diameter found today). Prior estimates based on the ejected volumes of material[6] yielded a slightly smaller transient diameter of $685 \pm 88\,\mathrm{km}$, which could indicate a lower speed impact. More recent estimates[27] based on the annular crustal bulge and numerical models also indicate a range of transient diameters ($\sim$500 km to 740 km) that depends on the thermal profile of the crust at the time. In this case, the numerical model assumed both a vertical impact at $15\,\mathrm{km\,s}^{-1}$ and a much smaller impactor diameter (80 km). Transient diameters estimated by other studies can be found in that study. The much larger diameter derived from the observations here suggests that three-dimensional models with a curved surface are needed to estimate the Imbrium transient crater diameter.

The derived transient rim diameters from the analytical scaling relations are also larger than recent estimates based on the positive gravity anomalies from the GRAIL mission and other gravity data[8]. This contradiction, however, can be reconciled if the interior gravity anomalies of Imbrium and other basins correspond to the shape and diameter of the deformed and displaced lower crust at depth[28,29], rather than a transient diameter referenced to the surface. Such an interpretation also would account for the offset of the gravity anomalies up range of the basin centre relative to the final basin rim, for example, Moscoviense, Orientale, Imbrium and Crisium[16].

Estimates for the transient crater diameters for other basins can be made based on other observed impactor diameters using the same approach described here[17]. For the peak-ring basin Schrödinger, the predicted transient apparent diameter is $\sim$200 km ($v = 25\,\mathrm{km\,s}^{-1}$, $\theta = 30°$) based on extrapolation from sand experiments[26] or 280 km for wet soil[19]. The observed (post-collapse) rim–rim diameter is 290 km; consequently, the latter calculation must represent an overestimate. Decreasing the speed to $15\,\mathrm{km\,s}^{-1}$ only partly corrects this discrepancy. For Moscoviense (445 km in diameter), an assumed impact speed of $25\,\mathrm{km\,s}^{-1}$ and a derived impactor diameter of 100 km in diameter yield nearly the same apparent transient crater diameters of 390 km (sand) and 380 km (wet soil). Both estimates, however, are unreasonable because rim collapse (25%) would increase the diameter beyond the observed diameter. Reducing the impact speed to $10\,\mathrm{km\,s}^{-1}$ (matching the hydrocode model) results in a rim–rim transient diameter of 350 km and collapsed rim of 440 km, which is close to the result from the CTH hydrocode model (485 km) for same inputs for projectile size, speed and angle.

The final diameter of Imbrium depends on the selected physical expression. For example, the outer diameter (1,250 km) is delineated from the northern shores of Mare Frigoris to the Apennines. It should be pointed out, however, that the transient crater diameter here ($\sim$830–860 km) is only about 3.5 times the impactor diameter. Such a small ratio reflects the role of gravity preventing ejecta from escaping the transient cavity. Nevertheless, high shock pressures extended well outside this limit and material still remained in motion, even though the crater would later collapse. Increasing the apparent transient diameter by 25% (for the transient rim–rim diameter) results in the calculated transient rim-to-rim basin diameter ranging from 1,040 km to 1,080 km, which would extend from the northwest rim of Sinus Iridum (region of first contact) to just inside the Apennines. The final crater, however, undergoes collapse. Up range (to the northwest), the transient crater profile would have been unstable due to over-steepening of the up-range wall and result in greater rim/wall collapse (for example, extending to Mare Frigoris). Shallower excavation down range[16], however, would have preserved the uplifted rim, now represented by the Apennines.

Surviving impactor fragments and the Late Heavy Bombardment. Laboratory impact experiments can be used to assess the size and state of fragments surviving oblique impacts. Oblique impacts into planar targets generate considerable down-range debris, largely derived from the impactor as recorded in witness plates placed down range[14]. Estimates for the size of the fragments can be derived from a combination of the size of the craters in a vertical witness plate (facing the debris down range) and the observed speed (from high-speed imaging) or the momentum generated by the collision. These experiments revealed two different processes: catastrophic disruption resulting in a strain-dependent power-law fragment size

distribution; and non-catastrophic disruption following a very different distribution revealed only at low impact angles ($<15°$). The strain dependence on the largest fragment size resembled the consequences for impact disruption of asteroids, the reverse of the case considered here. The non-catastrophic distribution, however, resulted in 5–8 similar size fragments travelling very close to the initial impactor speed. The sizes of these largest isolated fragments do not depend strongly on strain rate, consistent with these fragments formed by a different process (for example, shear)[14].

The derived sizes, however, do not represent the initial fragment dimensions following the first contact because they impacted the surface down range and fragmented still further, before impacting the witness plate. Hence, this approach underestimates the true projectile-fragment size distribution, except at the lowest impact angles ($<10°$). Impacting a sphere or cylinder, however, prevents some fragments impacting the surface down range[18]. Such experimental designs reveal that (1) some large fragments avoid re-impact with trajectories only slightly deflected from the initial trajectory, and (2) impacts into surfaces with sufficient curvature expose their true physical state and size following first contact (planar targets designed to avoid down-range impacts near the primary crater also preserve the original fragment sizes).

We further illustrate these results in a sequence of images that capture the size, trajectory and physical state of projectile fragments revealed in the high-speed image sequence shown in Fig. 2b and more completely in Extended Data Fig. 7. The 0.635-cm-diameter aluminium sphere impacted a 6.7-cm-diameter disk. Although the launch angle was actually 30° (from the horizontal), the impact point is slightly down range from the top, thereby resulting in an effective impact angle of 20° from the surface tangent on top of the disk. The collision resulted in about ten large fragments following close to the original trajectory, behind the vapour plume and jetting plasma. The largest fragment is about 0.2 cm in diameter, among other fragments 0.1–0.2 cm, consistent with measurements from impacted witness plates[14]. Smaller fragments leading this debris are cold (in silhouette) and near the initial trajectory, while others trail at slightly higher angles. In addition, a reddish glow surrounds this debris to either side of the trajectory and corresponds to a cloud of melt droplets. This distribution of debris is reflected in the arrival sequence observed on the witness plates with high-speed imaging.

The physical state of the Imbrium impactor after the collision depends on the impact angle and whether or not it fully decouples before hitting down range. In general, the peak pressure should reduce as $(\sin\theta)^2$ of the level for a vertical impact. For a 30° impact from the horizontal, this angle dependence means that the peak pressure would be reduced by a factor of 4. Two additional processes reduce the pressure even further. First, the density of the upper crust of the mega-regolith of the Moon reduces the impedance, thereby further reducing the peak pressure in the impactor. Second, the response in the impactor is more complicated than in the target because of the large amount of free surface, which reduces the expected peak pressures even further, along with the role of shear failure[18]. A prior modelling study[30] for a 5 km diameter at impact speeds comparable to this study for Imbrium ($20\,\mathrm{km\,s}^{-1}$) calculated peak pressures in the projectile during impacts into planar targets and found that a 30° impact allows 16% of the projectile to remain as a solid, whereas a 15° impact allows 100% to survive, generally consistent with laboratory experiments[14].

At the scale of the Imbrium basin, the widths of the parallel grooves down range provide a measure of the debris diameters based on crater scaling. At very low angle impacts ($<5°$) with speeds slightly less than the initial impactor speed, gravity-scaling relations for $10\,\mathrm{km\,s}^{-1}$ debris reveal that a 20-km-wide groove would have been produced by debris 4.5 km in diameter (equation (1)). At such low impact angles, however, groove widths should be controlled by strength scaling relations, which would predict even greater sizes for the debris. Grooves extending from near the region of first contact range from 10 km to 20 km across. Consequently, a conservative estimate predicts that some of the larger down-range fragments from the Imbrium impactor were conservatively 2 km to 4.5 km across, that is, less than 1–2% of the original diameter. Because a longer groove was probably not the result of a single impactor, grooves could represent more than one fragment while others could have escaped the Moon entirely.

If the impacting bodies were differentiated, the core would have a different distribution relative to the crust. For example, if the Moscoviense impactor was differentiated into a core and mantle, three-dimensional models reveal that projectile remnants line the interior ring while the crustal component is generally distributed beyond the rim[17]. This contrasts with prior results for the South Pole–Aitken basin, where the core is distributed beyond the rim[31]. The difference in distribution reflects the size of the impactor relative to the radius of the Moon.

More generally, recent studies indicate that ancient regolith breccias sampled at the Apollo 16 landing site have similar compositions (highly magnesian) poorly represented in current meteorite collections[21]. After the LHB, meteoritic contamination in the Apollo regolith shifted to a greater range of compositions. The

results of the study presented here suggest that the Imbrium impactor would have dispersed its signature across the Southern Highlands and account for the observed unique meteoritic contamination of Apollo 16 regolith preserved in regolith breccias, reflecting post-Imbrium reworking[32].

Consequently, large basin-forming collisions at angles less than 35° on the Moon (or any planet) should have generated considerable amounts of debris just from the surviving impactor mass that escaped the gravity field. The experiments, models and observations of groove width all show that this component should be composed of large masses (or weakly held masses) departing at speeds nearly the same as the original impact speed and along the original trajectory. This contrasts with excavated debris from the parent body that would have been heavily shocked to achieve comparable speeds and ejected over broad angles. Our observations indicate that the basin-forming impactors are much larger than those previously assumed to accommodate the surviving asteroids in the Hungaria region[21]. One important implication, then, is that this picture may be incomplete. For example, the E-belt dynamical model assumed an arbitrary number of test particles and then compared the fit of those dynamically surviving particles constrained by assumptions about crater and basin scaling. If our assessment is correct, then asteroids in the Hungaria region may be only a small fraction of the original total mass (and sizes), but not necessarily the number of bodies. Either the basin-forming bodies during the LHB did not all come from the proposed E-belt[33], or the E-belt was originally composed of larger bodies that underwent collisional fragmentation and dispersal during planet migration, a process that was acknowledged to be missing in that study.

23. McGlaun, J. M., Thompson, S. L. & Elrick, M. G. A three-dimensional shock wave physics code. *Int. J. Impact Eng.* **10,** 351–360 (1990).
24. Collins, G. S., Melosh, H. J. & Ivanov, B. A. Modeling damage and deformation in impact simulations. *Meteorit. Planet. Sci.* **39,** 217–231 (2004).
25. Senft, L. E. & Stewart, S. T. Dynamic fault weakening and the formation of large impact craters. *Earth Planet. Sci. Lett.* **287,** 471–482 (2009).
26. Schultz, P. H., Ernst, C. E. & Anderson, J. L. B. Expectations for crater size and photometric evolution from the Deep Impact Collision. *Space Sci. Rev.* **117,** 207–239 (2005).
27. Potter, R. W. K., Kring, D. A., Collins, G. S., Kiefer, W. S. & McGovern, P. J. Estimating transient crater size using the crustal annular bulge: insights from numerical modeling of lunar basin-scale impacts. *Geophys. Res. Lett.* **39,** L18203 (2012).
28. Schultz, P. H., Orphal, D. L., Miller, B., Borden, W. F. & Larson, S. A. in *Multi-Ring Basins* (eds Schultz, P. H. & Merrill, R. B.) Vol. 12A, 181–195 (1981).
29. Schultz, P. H. Atmospheric effects on ejecta emplacement and crater formation on Venus from Magellan. *J. Geophys. Res.* **97,** 16183–16248 (1992).
30. Pierazzo, E. & Melosh, H. J. Hydrocode modeling of oblique impacts: the fate of the projectile. *Meteorit. Planet. Sci.* **35,** 117–130 (2000).
31. Wieczorek, M. A., Weiss, B. P. & Stewart, S. T. An impactor origin for lunar magnetic anomalies. *Science* **335,** 1212–1215 (2012).
32. Korotev, R. L. Some things we can infer about the Moon from the composition of the Apollo 16 regolith. *Meteorit. Planet. Sci.* **32,** 447–478 (1997).
33. Minton, D. A., Richardson, J. E. & Fassett, C. I. Reexamining the main asteroid belt as the primary source of ancient lunar craters. *Icarus* **247,** 172–190 (2015).
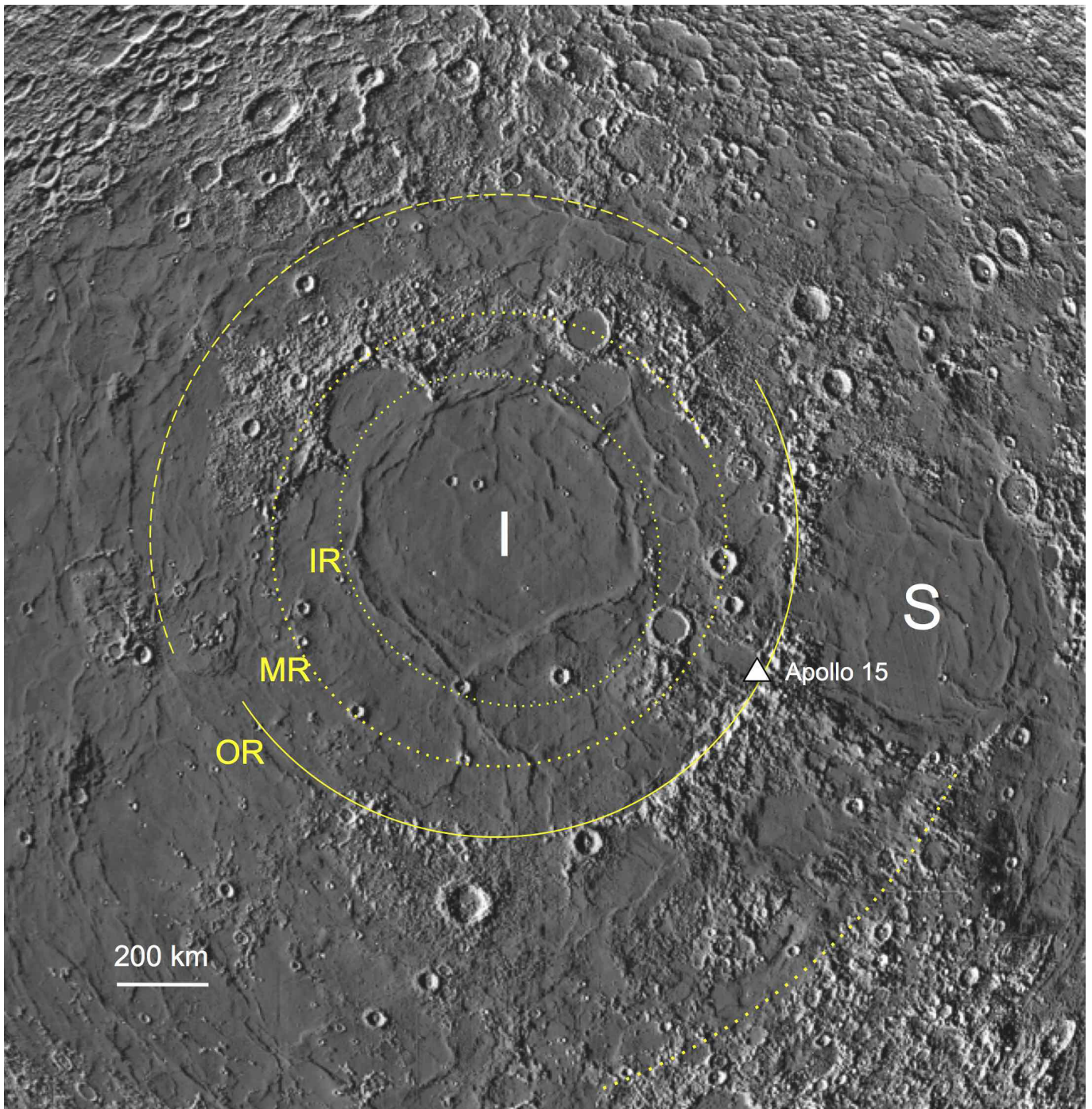
Extended Data Figure 1 | Mapped rings and features of the Imbrium basin that reveal asymmetries due to the impact trajectory and identify features for reference in the discussion. The rings comprising the Imbrium basin (I), including an outer ring, corresponding to the Apennines (OR), a middle ring extending to the Alpes Mountains (MR), and an oblong interior ring (IR) delineated by isolated massifs (mountains) and wrinkle ridges. An additional scarp-ring extends farther to the southeast (dotted line). The poorly expressed outer ring to the northwest is detached from the boundary to the southeast due to enhanced rim collapse in the up-range direction. The middle ring is incomplete but is recognized by isolated massifs and re-direction of tectonic features (wrinkle ridges). The inner ring is oblong (northwest–southeast) but truncated to the southeast. Nevertheless, wrinkle ridges do extend along the proposed trajectory. Such a pattern is consistent with portions of the impactor being decapitated after first contact but continuing to interact with the near surface down range. The Apollo 15 landing site at the base of the OR is also shown. 'S' indicates the Serenitatis basin. (Base map is an orthographic projection of Lunar Orbiter Laser Altimeter (LOLA) reproduced with permission from M. Collins.)
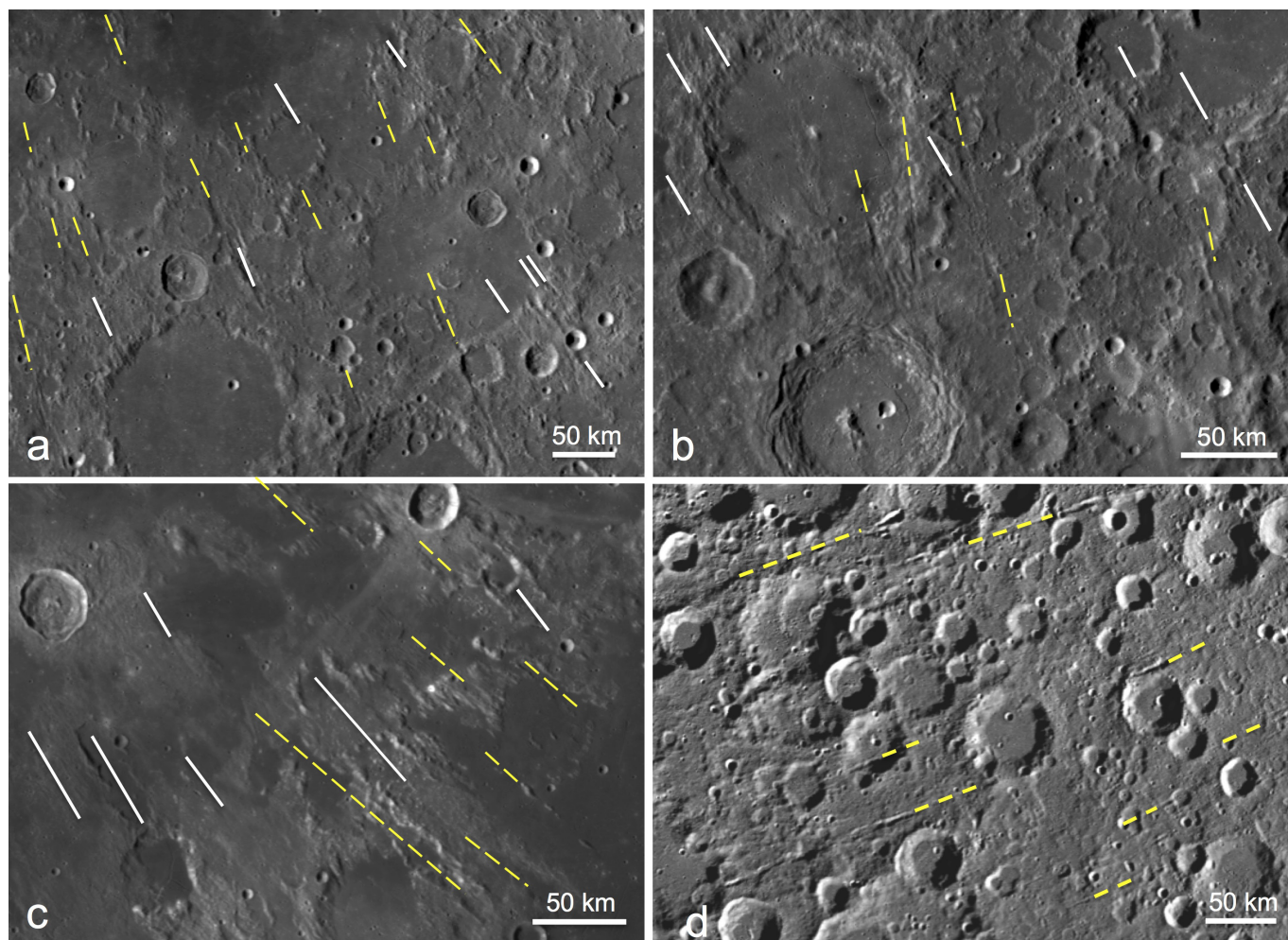
Extended Data Figure 2 | Mapped trends corresponding to grooves, scours and lineations in different directions around the Imbrium impact basin on the Moon. a, Region south–southeast of the Imbrium basin centred (latitude −6.693, longitude 6.491) near the trajectory line with the degraded crater Hipparchus in the right centre. White solid lines illustrate trends that converge up range of the basin centre (close to the point of first contact), whereas yellow dashed line trends converge closer to the centre of Imbrium (crater excavation). **b**, Region farther west from the trajectory line for Imbrium and south of Fig. 1a (centred at latitude −14.823, longitude −0.798). Certain grooves (white) have trends directed northwest (source up range of basin centre), and indicate first-arriving debris, in contrast to other sets (yellow), which are radial from the basin centre and correspond to later-arriving material. The crater Alphonsus is in the top left. **c**, Grooves and elongate secondaries near the Julius Caesar crater (bottom centre) and Boscovich craters (bottom left) southeast of Imbrium (latitude 12.496, longitude 15.681). Grooves/secondaries trending more northwest (solid white lines radial to the Imbrium) superpose those trending more westerly (dashed yellow lines converging on the proposed point of first contact). **d**, Region northwest (up range) of Imbrium (latitude, 68.304, longitude −114.03). The crater at the very top (only partial) is named Niepce. Most sets here indicate a source region towards the basin centre.
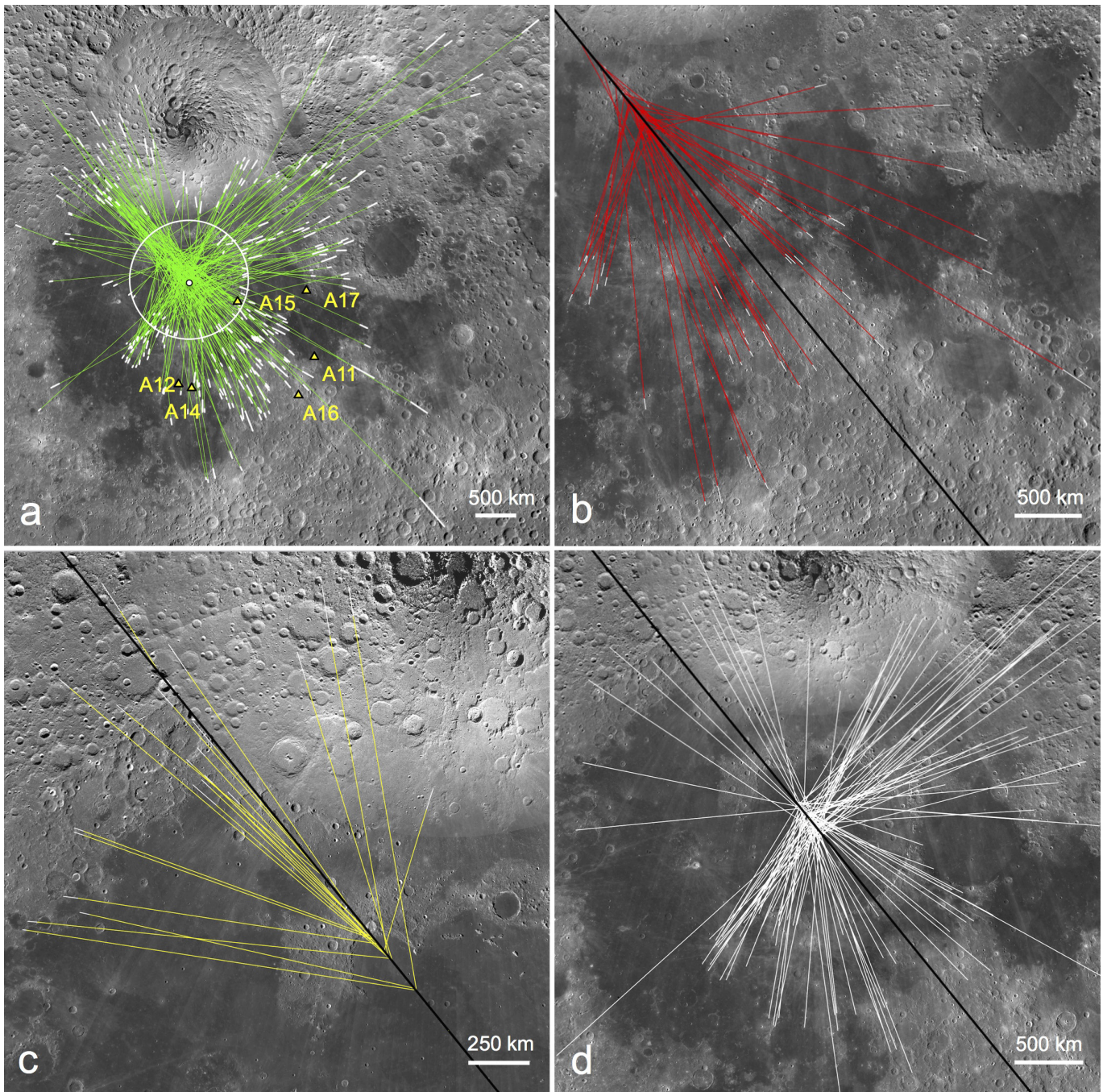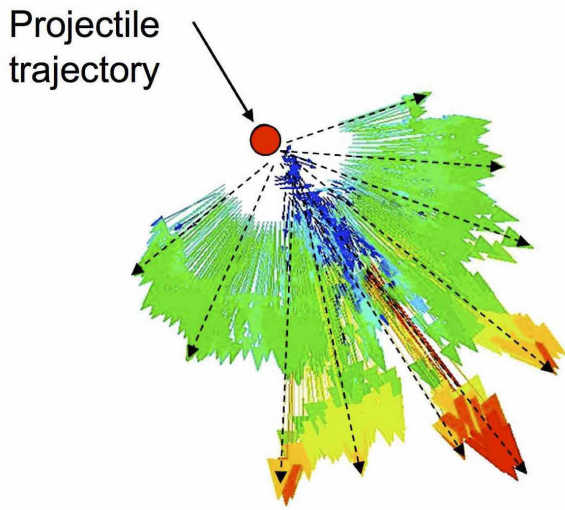
Extended Data Figure 3 | Mapped lineations extended as great circles into the Imbrium basin to assess sources during formation. a, Great circles extended from trends established by over 230 mapped grooves and elongate secondary craters related to the Imbrium basin (white circle). Locations of different Apollo landing sites are also identified. Lambert-conformal stereographic projection centred on Imbrium. **b**, Subset of trends from down-range secondaries that cross the trajectory more than 300 km northwest of the Imbrium centre. **c**, Subset of trends north of Imbrium intersecting the trajectory line well up range from the basin centre. **d**, Subset of great circles that cross the inferred Imbrium trajectory within a 300 km radius of its centre. The most distant secondaries have trends that converge slightly up range.
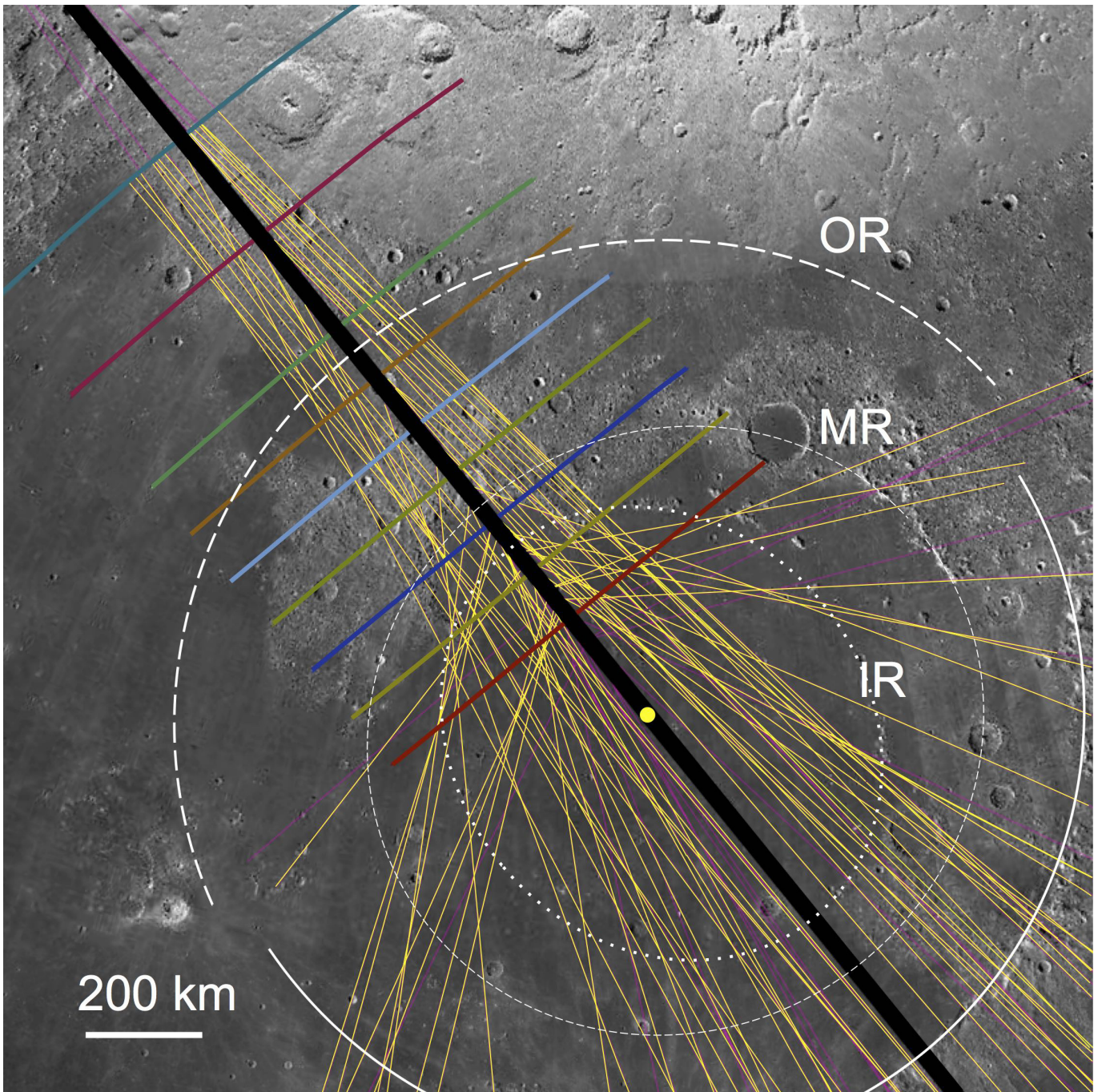
Extended Data Figure 4 | Subset of great circles of trends associated with down-range secondaries and grooves that cross the trajectory 300 km up range of its centre. One subset forms trends nearly paralleling the trajectory, consistent with sheared impactor fragments. Coloured lines orthogonal to the trajectory (bl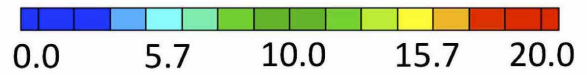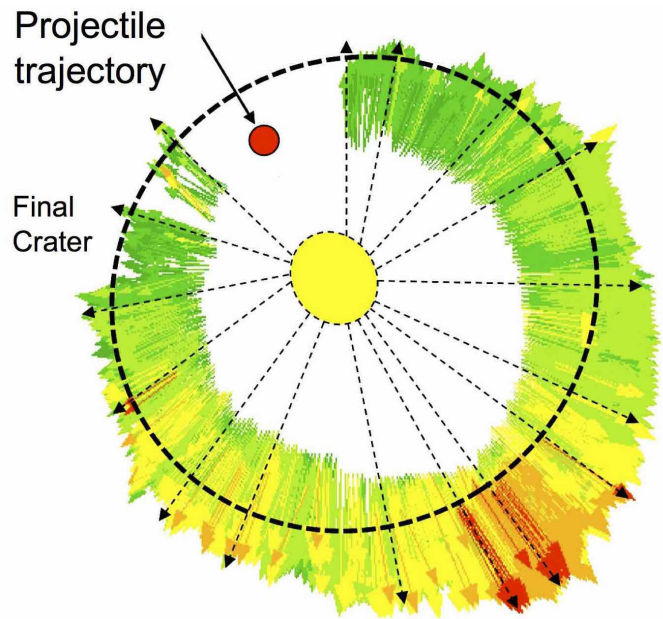ack) are used to constrain the size of the impactor (Fig. 3c). Circles correspond to basin rings defined by relict massifs and wrinkle ridges. IR, inner oblong ring; MR, middle ring; OR, outer ring, which is delineated by two different arcs resulting from the up-range rim collapse.

Projectile trajectory

Ejecta Velocity in Laser Plane (km/s)

a

Projectile trajectory

Final Crater

Ejecta Velocity in Laser Plane (km/s)

b

Extended Data Figure 5 | Evolution of trajectories from hypervelocity oblique impact experiments, illustrating the evolving source region during excavation. a, Early trajectory. **b**, Late trajectory. Packets of ejecta passing through a horizontal laser beam (using three-dimensional particle velocimetry) were captured in multiple cameras to establish in-flight trajectories at different times of crater growth. Modified from ref. 13 (**a**) and ref. 11 (**b**).

a

b

c
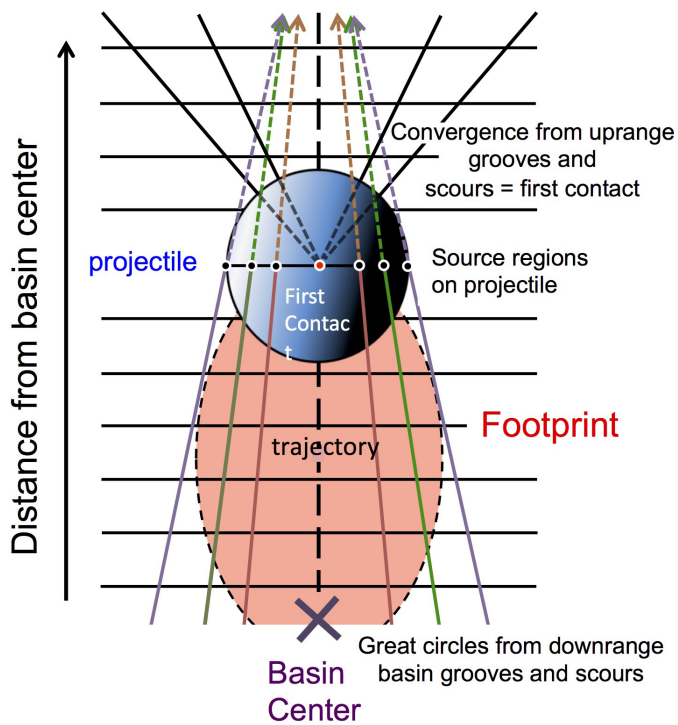
Extended Data Figure 6 | Strategies for determining the position of the impact point from mapped patterns on a target surface.
a, Mapped trends of grooves and elongated trajectories down range that do not converge near the crater centre allow estimation of the size of the projectile. Convergence of trends from the up-range direction constrains the region of first contact. Convergence of trends intercepting a line orthogonal to the trajectory at the location set by the region of first contact constrains the diameter of the projectile. b, c, Convergence diagrams for 15° (b) and 30° (c) hypervelocity impacts into aluminium by 0.635 cm
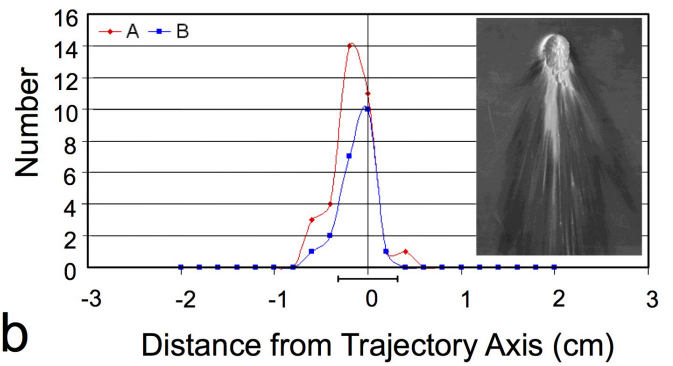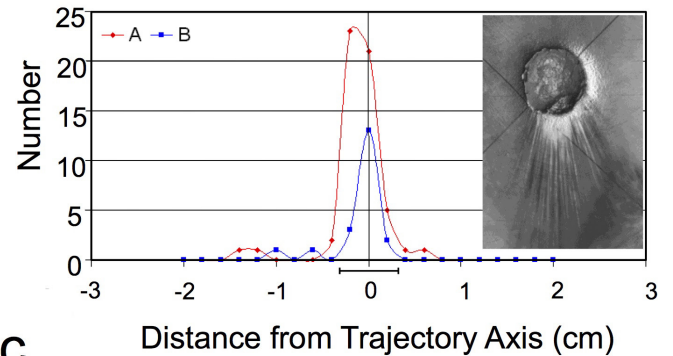
aluminium spheres onto planar targets. Grooves created by hypervelocity projectile debris converge and cross a reference line perpendicular to the trajectory at the up-range rim of the crater (line A) and 1.5 projectile diameters up range (line B). Well beyond the up-range rim (line B), the spray originates from spalls and shears from either side of the projectile and travels down range with little relative velocities directed away from the initial trajectory. Therefore, these components can be used to estimate the impactor diameter, consistent with 0.635 cm (indicated by the scale bar below).
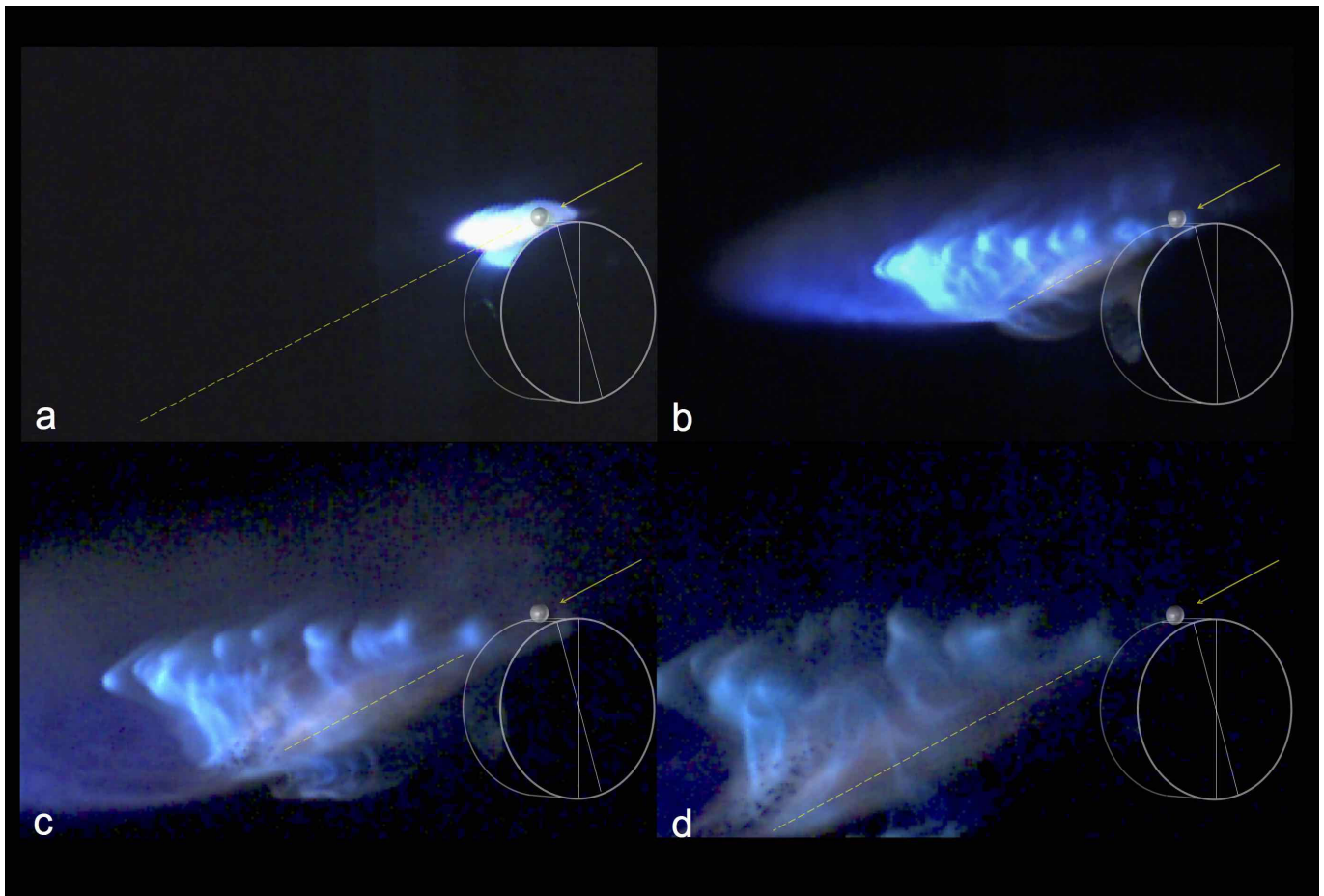
Extended Data Figure 7 | Fragmental debris resulting from a 0.635 cm aluminium sphere impacting a 6.7 cm aluminium disk at ~5 km s⁻¹. a–d, The launch angle was 30°, but because the impact point was not at the top of the disk, the actual impact angle was 20°. **a**, The top left frame shows the jetting phase (blue–white tongue-like extension). **b**, The jetting phase (15 μs later) shows the jetting phase, now a faint blue haze, and vapour (turbulent blue gas) with fragments emerging near and above the yellow dashed line (the crater seen below the impact on the disk was from a prior experiment). **c**, Still later, leading fragmental debris down range (near the yellow dotted line immersed in plasma) separate from the vapour phase along the initial trajectory. **d**, The fourth frame shows 8–10 large fragments (1–3 mm across) travelling close to the same speed as the initial impactor. Experiments were performed without artificial illumination and shows that the fragments are not notably heated. The aluminium sphere is represented graphically, and the aluminium disk is faintly outlined.
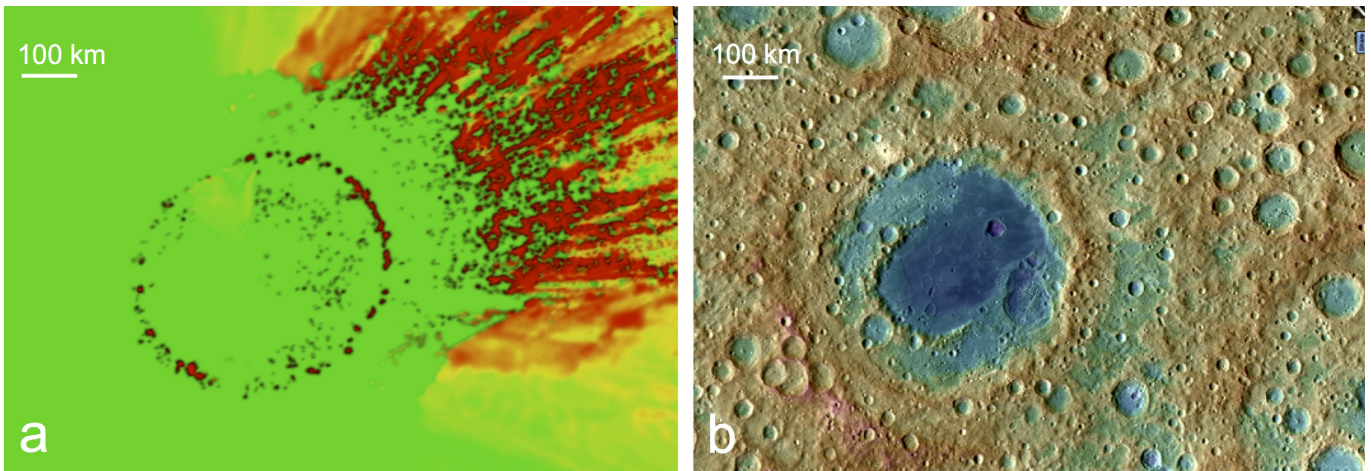
Extended Data Figure 8 | Comparing results of the CTH numerical model and the Moscoviense basin on the Moon from corresponding LOLA-DEM data without mapped lineations. a, The CTH model tracked where impactor fragments intersected the surface (in red). Beyond the rim, the linear red areas point towards the region of first contact, rather than the centre of the basin. See Fig. 3a for mapped lineations. Later ejecta (not shown) cover this evidence as identifiable units but their effects (grooves) remain preserved. **b**, The shaded relief map from the Lunar Laser Altimeter is shown here without the mapped lineations shown in Fig. 3b. Mapped lineations in Fig. 3b were based not only on topographic data but available images from Lunar Orbiter, Apollo and LROC wide-angle cameras.

Extended Data Table 1 | Comparison of selected transient basin diameters calculated from two scaling equations

Basin	Assumed impact speed	Actual rim-rim diameter (km)	Impactor diameter* (km)	Sand[†]		Wet Sand[‡]	
				D_{tA} (km)	D_{tR} (km)	D_{tA} (km)	D_{tR} (km)
Schrödinger		290	45				
	25 km/s			200	(250)	(280)	(440)
	15 km/s			170	210	230	350
Moscoviense		445	100				
	25 km/s			(390)	(480)	(380)	(480)
	15 km/s			320	(400)	(340)	(420)
	10 km/s			280	350	280	350
Orientale		930	110				
	25 km/s			420	520	460	570
	15 km/s			350	440	360	460
Imbrium		1250	250				
	25 km/s			830	1040	860	1080
	15 km/s			700	880	690	860

D_{tA} is the apparent transient crater diameter (referenced to the pre-impact surface). D_{tR} approximates the rim–rim transient crater (pre-collapse); rim collapse increases the diameter by another 25%. Parentheses indicate unreasonable values. Impact angles are assumed to be at 30° (except where noted). Values are rounded to two figures.
*Estimates for impactor diameter for Schrödinger and Orientale are from ref. 17.
†Constants and exponents from ref. 27.
‡Constants and exponents from ref. 19.